A simple model of chaotic advection and scattering

Gustavo Stolovitzky
Center for Studies in Physics and Biology, Rockefeller University, New York, New York 10021

Tasso J. Kaper
Department of Mathematics, Boston University, Boston, Massachusetts 02215

Lawrence Sirovich
Center for Studies in Physics and Biology, Rockefeller University, New York, New York 10021
and Division of Applied Mathematics, Brown University, Providence, Rhode Island 02912

(Received 14 December 1994; accepted for publication 16 June 1995)

In this work, we study a blinking vortex-uniform stream map. This map arises as an idealized, but essential, model of time-dependent convection past concentrated vorticity in a number of fluid systems. The map exhibits a rich variety of phenomena, yet it is simple enough so as to yield to extensive analytical investigation. The map's dynamics is dominated by the chaotic scattering of fluid particles near the vortex core. Studying the paths of fluid particles, it is seen that quantities such as residence time distributions and exit-vs-entry positions scale in self-similar fashions. A bifurcation is identified in which a saddle fixed point is created upstream at infinity. The homoclinic tangle formed by the transversely intersecting stable and unstable manifolds of this saddle is principally responsible for the observed self-similarity. Also, since the model is simple enough, various other properties are quantified analytically in terms of the circulation strength, stream velocity, and blinking period. These properties include: entire hierarchies of fixed points and periodic points, the parameter values at which these points undergo conservative period-doubling bifurcations, the structure of the unstable manifolds of the saddle fixed and periodic points, and the detailed structure of the resonance zones inside the vortex core region. A connection is made between a weakly dissipative version of our map and the Ikeda map from nonlinear optics. Finally, we discuss the essential ingredients that our model contains for studying how chaotic scattering induced by time-dependent flow past vortical structures produces enhanced diffusivities. © *1995 American Institute of Physics.*

I. INTRODUCTION

Recent simulations of high Reynolds number *box turbulence* indicate the presence of linear structures of intense vorticity, see Siggia [1981], She *et al.* [1990], and Zabusky *et al.* [1993]. Inviscid models of such structures are point vortices. Further, in any turbulent flow, physical or numerical, such intense vortical motion exists in the presence of irregularly occurring large scale eddy motions that sweep past, as well as convect, the filaments of vorticity. In an attempt to model particle paths in these types of fluid flows, we consider the highly idealized situation of a single point vortex in the presence of a uniform stream that undergoes unidirectional oscillation under a square wave duty cycle, as does the vortex strength. This model exhibits a wealth of interesting phenomena and simultaneously yields to extensive analytical investigation. Furthermore, it may be the simplest fluid mechanical model in which chaotic dynamics appears.

The model that we consider is related to the blinking vortex model introduced by Aref [1984] and further studied by Doherty and Ottino [1988] (see also Chap. 7 in Ottino [1989]). In the Aref model, co-rotating vortices of equal strength are alternately turned on and off under a square wave duty cycle. The effect of one vortex on the other is, to a first approximation, that of a locally uniform flow, and our model is thus related to that of the blinking vortices.

The model considered here may be made more realistic by allowing for randomness in the velocity, vortex strength and the time dependence in the duty cycle, and by examining more complicated types of vortices such as patches or vortices with finite cores; however, these additions would come at the expense of the simplicity of the model. Also, as in chaotic dynamics in general, one must be cautious in interpreting the results within the framework of turbulence, see for instance the discussion in Aref [1990]. At each instant one sees the generated flow as being laminar. Only the particle paths themselves exhibit chaotic behavior. While this may shed light on the mixing process inherent in turbulent flows, the dynamics lacks essential features of turbulence, principally vortex stretching. Nevertheless, Pierrehumbert [1992] has employed model problems with chaotic convection to investigate scalar spread in the turbulent atmosphere.

The model considered here exhibits chaotic scattering behavior for a wide range of uniform stream velocities, circulation strengths, and blinking periods. This behavior is manifested by the presence of fluid particles initially approaching the point vortex that scatter off of it in a chaotic fashion. Measurements are made of both the positions of these particles as they exit the vortex region and the lengths of the time intervals these particles spend in the core region, the so-called residence times. Our measurements show that these quantities depend sensitively on the initial position of the incoming particle and that they scale in self-similar fashions.

The main geometrical structures responsible for the ob-

served chaotic scattering are the principal saddle fixed point of the map along with the homoclinic tangle attached to it. The principal saddle fixed point is created by a bifurcation at infinity that results when the velocity of the uniform stream changes from being zero to being positive. An analysis of this bifurcation, as well as of the dynamics near infinity, is carried out using the technique of Poincaré compactification.

For the positive interval of control parameters in which this principal saddle fixed point exists, one branch of each of its stable and unstable manifolds asymptote to infinity. The other branches intersect each other transversely and, thus, form a homoclinic tangle. For a theoretical treatment of these concepts from the global theory of dynamical systems, see Guckenheimer and Holmes [1983], and for one of the earliest applications of these concepts to fluid mechanical problems see Rom-Kedar *et al.* [1990]. If the blinking period and the circulation strength are held constant, then one observes that: (i) the distance from the fixed point to the center of the vortex scales inversely with the velocity of the uniform stream; and (ii) the width of the homoclinic tangle grows with increasing uniform stream velocity, and this dependence is highly nonlinear. This detailed scaling information about the geometrical structure reveals the reason for the observed sensitive dependence and self-similarity in the chaotic scattering measurements.

For other studies of chaotic scattering in physical systems—both classical and quantum—see for example the special issue of *Chaos* [Vol. 3, No. 4, (1993)] devoted to this subject (in particular the introduction by Ott and Tel [1993]) and the references cited in those works. Also see Bleher *et al.* [1990]. Finally, the problem studied in Kadke and Novikov [1993], although very different in scope from that of the present paper, has several similar features.

A noteworthy feature of the model is that the location of all fixed points and many periodic points can be determined analytically. We take advantage of this to show that the map exhibits many conservative period-doubling cascades. As the velocity of the uniform stream is decreased from certain critical values, stable periodic points become unstable (hyperbolic with reflection), and in so doing, they shed pairs of new stable periodic points of twice the period. An estimate of the Feigenbaum universal constant for this model, based on a limited number of period-doubling events, is near the conservative Feigenbaum number, $\delta_F \approx 8.72$. This conservative version of universality has been studied in many area-preserving maps, most notably in the quadratic De Vogeleare map, see for example Helleman [1980], Collet *et al.* [1981], Greene *et al.* [1981], and the exposition of Fermi acceleration in Section 3.4 of Lichtenberg and Lieberman [1983].

A further feature of the model is that the map may be reformulated as a Hamiltonian system consisting of the stream function for a pure point vortex subject to a periodic series of delta function kicks. The periodic delta function kicks are equivalent to the action of the uniform stream that transports particles unidirectionally for half of the duty cycle. This reformulation enables us to determine the resonant dynamics inside the principal homoclinic tangle in a fairly complete way. There are both inner and outer core regions. The outer core region is that region containing the resonance bands formed by the principal $m:1$ (and $m:n$) subharmonic periodic points. In contrast, the inner core region is that region containing the $1:n$ (and $m:n$ for $m<n$) superharmonic points. Each of these regions may also contain KAM tori, and higher order island chains, but the important result is that they are well-defined regions in the fluid domain. Moreover, the width of these resonances is obtained analytically in asymptotic form, and the Chirikov resonance overlap criterion (Chirikov [1979]) is applied to determine the threshold parameter values for which some pairs of resonances overlap. These overlap thresholds determine the extent to which particles can penetrate close to the center of vorticity.

For examples of other works in which the dynamics governed by oscillators are subject to delta function kicking, we refer the reader to Zaslavsky [1991] where the formation of stochastic webs is presented, and to Cecchi *et al.* [1993] where the oscillators under study are hard relaxation oscillators.

Finally, we examine the change in behavior fluid particles undergo when the vortex changes from being a pure point vortex to a weakly entraining point vortex. These vortices weakly entrain fluid particles into the core region. Numerically it is found that strange attractors appear in the fluid flow. These attractors seem to be the closures of the unstable manifolds of the saddle fixed points. Yu *et al.* [1990, 1991] study the fractal properties of the attractors that arise in a random map modeling particles floating on surfaces. Their map is derived from an incompressible three-dimensional fluid in which the third velocity component contains a periodic sequence of delta functions and makes a nonzero contribution to the divergence of the full velocity field, so that the flow restricted to the surface is compressible. Moreover, Yu *et al.* [1990] point to other fluid mechanical problems in which weakly-compressible flows can occur. Also, Zaslavkii and Rachko [1979] and Zaslavsky [1978] study equations with a periodic sequence of delta functions and they also find the formation of strange attractors. However, their model is designed to analyze the onset of turbulence and it consists of a single mode with a stable limit cycle in which the kicks represent the cumulative effect of all of the other modes.

The paper is organized as follows. In Sec. II, we formulate the map and present the time-continuous version of it. The period-doubling cascades, emanating from the fixed points, are found in Sec. III. The global dynamics of the map are studied in Sec. IV. These global properties are then used in Sec. V to analyze the chaotic scattering phenomena associated to this blinking flow. In Sec. VI, we study the superharmonic resonances in the core region. Further, in Sec. VII, we present the analysis of the bifurcation of the principal fixed point at infinity. In Sec. VIII, we briefly analyze the case of weakly attracting point vortices. Finally, in Sec. IX, we discuss the physical relevance of our model and summarize our main results. The appendices contain various useful calculations.

II. FORMULATION OF THE MAP

We consider the flow generated by a point vortex of strength κ located at the origin and turned on for a time duration $T/2$. At $t=T/2$ the vortex is turned off and a uni-

form stream of velocity V in the positive x-direction is turned on for a duration $T/2$. This cycle is then repeated indefinitely.

With the complex variable z used to define a coordinate system in the two-dimensional fluid domain, the complex potential of the vortex motion is given by

$$w_1(z) = -\frac{i\kappa}{2\pi} \ln z, \tag{2.1}$$

and that of the uniform flow by

$$w_2(z) = Vz. \tag{2.2}$$

Therefore, if a fluid particle is initially at z_0, then it is located at

$$z_{1/2} = z_0 \exp\left[\frac{i\kappa}{2\pi|z_0|^2}\frac{T}{2}\right]$$

at the end of a half cycle, and at

$$z_1 = z_{1/2} + \frac{VT}{2}$$

at the end of a full cycle. This area-preserving, conformal mapping is invariant under $T \to -T$, $V \to -V$, $\kappa \to -\kappa$.

We nondimensionalize the position variable z by setting $z' = z/L$, where the length scale $L = \frac{1}{2}\sqrt{\kappa T/\pi}$ is the radius of that circle on which a particle rotates through one radian in a time interval of length $T/2$. When primes are dropped, the map is

$$z_1 = z_0 \exp\left[\frac{i}{|z_0|^2}\right] + \epsilon. \tag{2.3}$$

Here the single dimensionless control parameter (see Appendix A for an alternative parametrization) in the problem is

$$\epsilon \equiv \sqrt{\frac{T\pi V^2}{\kappa}} = \frac{L_0}{L}, \tag{2.4}$$

where $L_0 = (1/2)VT$ is the distance a particle is carried by the uniform stream in time $T/2$. Since κ carries the same units as diffusivity, ϵ^2 can loosely be thought of as a ''Reynolds'' number.

Formally the map is

$$z_{n+1} = z_n \exp\left[\frac{i}{|z_n|^2}\right] + \epsilon. \tag{2.5}$$

Clearly, the particle can be returned to its initial position by a translation of $-\epsilon$, followed by a clockwise rotation. Hence, the inverse map is given by:

$$z_n = (z_{n+1} - \epsilon) \exp\left[\frac{-i}{|z_{n+1} - \epsilon|^2}\right].$$

It follows from (2.5) that

$$|z_{n+1} - \epsilon| = |z_n|,$$

and that, therefore, the line $\mathrm{Re}(z) = \epsilon/2$ is a line of symmetry of the map. Exploiting this symmetry and simultaneously simplifying the analysis of the map, we introduce the transformation:

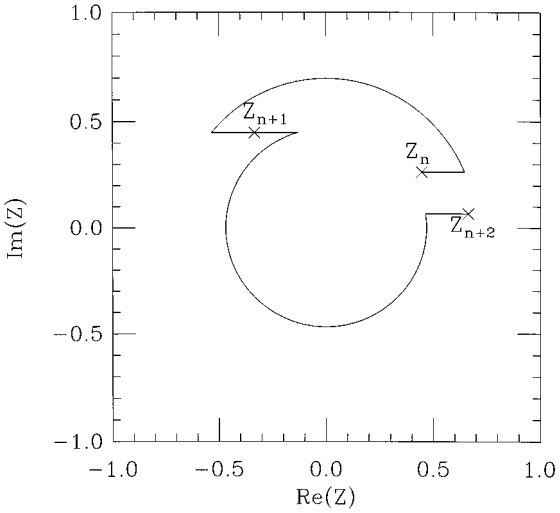

FIG. 1. Motion of a fluid particle under the map (2.7).

$$z = \mathcal{Z} + \frac{\epsilon}{2}. \tag{2.6}$$

In terms of $\mathcal{Z}$, the map becomes:

$$\mathcal{Z}_{n+1} = M\mathcal{Z}_n \equiv \left(\mathcal{Z}_n + \frac{\epsilon}{2}\right) \exp\left[\frac{i}{|\mathcal{Z}_n + \epsilon/2|^2}\right] + \frac{\epsilon}{2} \tag{2.7}$$

and the inverse map is

$$M^{-1}\mathcal{Z}_{n+1} \equiv \left(\mathcal{Z}_{n+1} - \frac{\epsilon}{2}\right) \exp\left[\frac{-i}{|\mathcal{Z}_{n+1} - \epsilon/2|^2}\right] - \frac{\epsilon}{2}. \tag{2.8}$$

This new format, which is the form of the map we shall use throughout this work, represents a quarter wavelength shift in the duty cycle compared to that of (2.5) see Fig. 1. A fluid particle is advanced first by a shift to the right of $\epsilon/2$, then by an appropriate counterclockwise rotation and finally by another translation to the right of $\epsilon/2$, completing the cycle. Even though the formulation (2.7) looks more cumbersome than the original map (2.5), it has the important advantage that the symmetry line is now conveniently $\mathrm{Re}(\mathcal{Z}) = 0$. Also, as a consequence of the symmetry, reflection in $\mathrm{Re}(\mathcal{Z}) = 0$ of the inverse map on the similarly reflected point is the same as the action of M on the point itself:

$$M\mathcal{Z} = -[M^{-1}(-\mathcal{Z}^*)]^*,$$

where $*$ denotes complex conjugate. Moreover, iteration yields: $M^k(\mathcal{Z}) = [-M^k(-\mathcal{Z}^*)]^*$. Thus, if we follow the seed point $\mathcal{Z}_0$ forward *in time* and the seed $-\mathcal{Z}_0^*$ backward in time we obtain trajectories that are reflections of one another in $\mathrm{Re}\,\mathcal{Z} = 0$.

Finally, for several purposes, it is convenient to have a time-continuous version of the map:

$$\dot{\mathcal{Z}}^* = \frac{\partial}{\partial \mathcal{Z}}\left[-i \ln \mathcal{Z} + \epsilon\mathcal{Z}\sum_{k=-\infty}^{\infty}\delta(t-k)\right]$$

$$= \frac{\partial}{\partial \mathcal{Z}} F(\mathcal{Z}). \tag{2.9}$$

Under the dynamics of (2.9), a fluid particle initially ($t=0$) at $\mathcal{Z}_0$ gets convected to the point $\mathcal{Z}_0+\epsilon/2$ in between times $t=0$ and $t=0^+$ by the uniform stream, then it is swept through an angle $1/|\mathcal{Z}_0+\epsilon/2|^2$ on a circle of radius $|\mathcal{Z}_0+\epsilon/2|$ in a unit time, and finally in between times $t=1^-$ and $t=1$ it gets translated to the right by an amount $\epsilon/2$, yielding precisely the mapping M in (2.7).

The system (2.9) is a time-periodic, one-degree-of-freedom system (often referred to as a one-and-a-half degree of freedom system) in which the Hamiltonian for a point vortex receives periodic kicks of magnitude ϵ. The imaginary part of the complex potential $F(\mathcal{Z})$, i.e. the streamfunction, is the Hamiltonian for the flow of (2.9):

$$H(\mathcal{Z},t)=-\ln|\mathcal{Z}|+\epsilon\ \mathrm{Im}(\mathcal{Z})\sum_{k=-\infty}^{\infty}\delta(t-k). \qquad (2.10)$$

With this formulation, we regard the periodic *kicking* as a perturbation to the otherwise periodic circular motion engendered by purely vortical motion, although the control parameter ϵ in (2.7) should not necessarily be regarded as small.

III. HIERARCHIES OF FIXED POINTS AND PERIODIC ORBITS

As explained above, fixed points of the map (2.7) must lie on the line $\mathrm{Re}(\mathcal{Z})=0$. This may be seen directly from the symmetry of the map or by observing that (2.7) implies $|\mathcal{Z}_f-\epsilon/2|=|\mathcal{Z}_f+\epsilon/2|$, where $\mathcal{Z}_f$ denotes the fixed point. Thus, when $\epsilon>0$ and a fixed point exists, we may set:

$$\mathcal{Z}_f\equiv i\,\frac{\delta}{2}, \qquad (3.1)$$

where δ is a real number, and it follows from (2.7) that

$$i\delta=(i\delta+\epsilon)\ \exp\left[\frac{4i}{\delta^2+\epsilon^2}\right]+\epsilon.$$

Finally, taking moduli and simplifying using trigonometric identities, we arrive at an implicit transcendental equation for δ as a function of ϵ:

$$\frac{\epsilon}{\delta}=\tan\left[\frac{2}{\epsilon^2+\delta^2}-\pi l\right], \qquad (3.2)$$

where l is a non-negative integer and where the convention we adopt is that the argument of the tangent function must lie in between 0 and π.

Plots of these fixed points are shown in Fig. 2(a) for $l=0$ and in Fig. 2(b) for $l=1,...,5$. Stable branches are indicated by continuous lines and unstable branches by dashed lines. At any fixed point $\mathcal{Z}_f=i(\delta/2)$, the linearized map has eigenvalues

$$\lambda_{1,2}=E\pm\sqrt{E^2-1}, \qquad (3.3)$$

where $E\equiv\cos\beta+\beta\sin\beta$, and $\beta\equiv 4/(\delta^2+\epsilon^2)$.

Next, we turn to the location of these fixed points, and the trajectories they execute during one iteration of the map. The paths for the upper and lower branch $l=0$ and $l=1$ fixed points are shown in Fig. 2(c). The upper branch $l=0$ fixed point gets mapped to the point $i(\delta/2)+(\epsilon/2)$ by the action of the blinking uniform flow during the first quarter of the duty cycle. Then it is transported around on the arc of a large circle of radius $|i(\delta/2)+(\epsilon/2)|$ to the point $i(\delta/2)-(\epsilon/2)$ by the blinking vortex. Finally, it is returned to its starting position during the last quarter of the duty cycle by the uniform flow, and is therefore, a fixed point of the map (2.7). Due to its central role in the dynamics of the map M, we refer to this point as the principal fixed point, and denote it by $\mathcal{Z}_{pf}$. That it is a saddle, and hence unstable, follows since $E^2>1$ there.

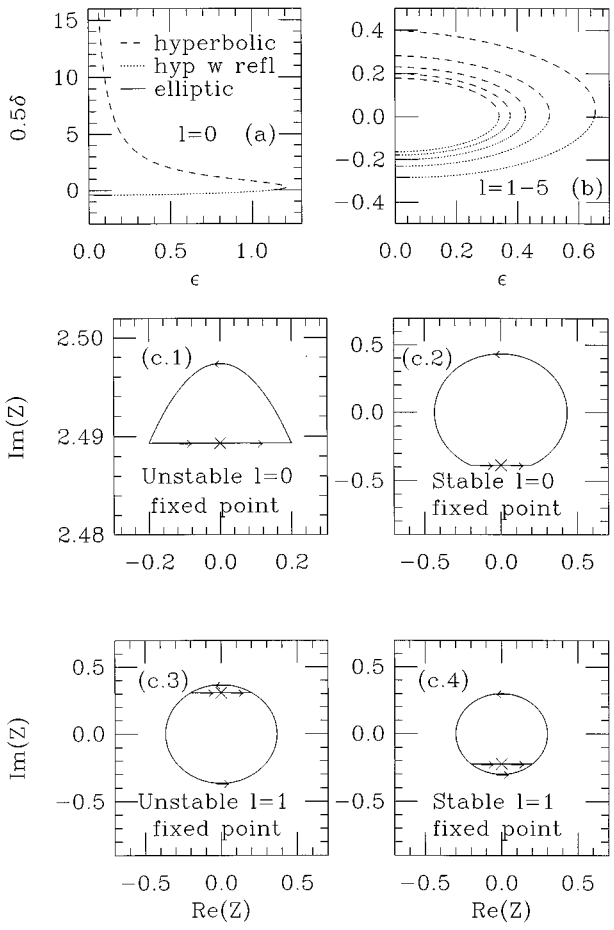

FIG. 2. (a) The $l=0$ branch of fixed points, given by formula (3.2). (b) the $l=1,...,5$ branches of fixed points, given by formula (3.2); the value of l increases going inwards. (c) Four panels showing the trajectories executed during one iteration of the map with $\epsilon=0.4$ by the $l=0$ upper and lower branch fixed points (c.1 and c.2), and by the $l=1$ upper and lower branch fixed points (c.3 and c.4).

By contrast, the lower branch $l=0$ fixed point follows a circle of much smaller radius, and makes almost one complete revolution before returning to its starting point with $\delta<0$. Next, the upper branch $l=1$ fixed point makes slightly more than one complete revolution around a circle during the middle of the duty cycle [traversing the upper arc in between the points $i(\delta/2)+(\epsilon/2)$ and $i(\delta/2)-(\epsilon/2)$ twice], and the radius of this circle is slightly smaller than that of the stable $l=0$ fixed point. It is also unstable and $\delta>0$. Finally, the lower branch $l=1$ fixed point (for which $\delta<0$) executes almost two complete revolutions about an even smaller circle; see the fourth panel. In fact, it traverses all but the bottom arc of that circle twice.

For a general $l=L$, the trajectory of the upper branch (regular hyperbolic) fixed point executes slightly more than L complete revolutions around a circle, and the trajectory of the lower branch fixed point makes almost $L+1$ complete revolutions around a smaller circle.

Furthermore, the locations of the fixed points in the limit of $\epsilon \to 0$ are clear from the pictures of their trajectories during one duty cycle, as shown in Fig. 2(c). The $\epsilon=0$ asymptotic location of $\mathscr{Z}_{pf}$ is

$$\mathscr{Z}_{pf} \sim i\,\frac{1}{\epsilon}$$

since we know from (3.2) that $\delta/2 \sim 1/\epsilon$ as $\epsilon \to 0$. See also Fig. 2(a).

In the limit of $\epsilon=0$, the lower branch $l=0$ and the upper branch $l=1$ fixed points are located exactly on the intersection of the imaginary axis with the circle $|\mathscr{Z}|^2=1/2\pi$, namely, at $i(\delta/2)=-(1/\sqrt{2\pi})i \approx -0.3989i$, and at $i(\delta/2)=(1/\sqrt{2\pi})i \approx 0.3989i$, respectively. Therefore, noting that every point on the circle $|\mathscr{Z}|^2=1/2\pi$ is a fixed point in the $\epsilon=0$ version of the map (2.7), we observe that the lower branch $l=0$ fixed point and the unstable $l=1$ fixed point are precisely the two points from this entire circle of fixed points which persist for $\epsilon>0$. This is the well-known Poincaré–Birkhoff picture.

Similarly, in the limit of $\epsilon=0$, the stable $l=1$ and the unstable $l=2$ fixed points are located exactly on the intersection of the imaginary axis with the circle $|\mathscr{Z}|^2=1/4\pi$, namely, at $i(\delta/2)=-(1/\sqrt{4\pi})i \approx -0.2821i$, and at $i(\delta/2)=(1/\sqrt{4\pi})i \approx 0.2821i$, respectively. They are the only two points from the entire $\epsilon=0$ circle of fixed points at $|\mathscr{Z}|^2=1/4\pi$ that persist for $\epsilon>0$. In general, in the limit of $\epsilon=0$, we have $|i(\delta/2)|=(1/\sqrt{2\pi L})$ for both the $l=L-1$ stable fixed point and the $l=L$ unstable fixed point, see Fig. 2(b).

Moreover, for each l, there exists a value of ϵ at which the pair of lower and upper branch fixed points corresponding to that value of l coalesce and disappear in a saddle–node bifurcation. We shall denote this value, which may be found by solving $(d\epsilon/d\delta)(\epsilon_l)=0$, by ϵ_l, and we observe that the corresponding δ for which (3.2) holds is positive. As discussed above, for example, $\epsilon_{l=0} \approx 1.2038$, and neither of the two $l=0$ fixed points exist for $\epsilon > \epsilon_{l=0}$, as is shown in Fig. 2(a). Furthermore, Fig. 2(b) shows that the range in ϵ for which the lth fixed points exist decreases as l increases.

It is clear from Fig. 2(a) and 2(b) that as ϵ is increased from zero, stable fixed points lose their stability and become hyperbolic with reflection. In the process, a pair of stable period-2 points are created. For each of the l branches, this bifurcation occurs at a different value of ϵ. At the bifurcation, a horizontal figure-of-eight shape is born (the separatrix) and the new elliptic points are created inside the loops of the figure-of-eight, such that their location is $\xi + i\eta$ and $-\xi + i\eta$. The strategy for computing ξ and η is given in Appendix B. An interesting question is whether these bifurcations are the first steps in conservative period-doubling cascades. However, we found these branches of stable period-2 points could be continued for a wide range of ϵ values, and we did not observe any further bifurcation of the elliptic period-2 points, although we have not been able to prove this.

Interestingly, we observed the first four steps in what appears to be a conservative period-doubling cascade as ϵ is decreased from the values ϵ_l. From above, we recall that at ϵ_l a stable and unstable fixed point coalesce in a saddle–node bifurcation. Their location at ϵ_l is $i(\delta_l/2)$, where $\delta_l > 0$. When ϵ is decreased from ϵ_l, the stable fixed points approach the origin. When the corresponding value of δ reaches zero, the fixed points become hyperbolic with reflection, as is readily seen in Eq. (3.2). In effect, when $\delta \to 0$, Eq. (3.2) implies that

$$\frac{2}{\epsilon^2+\delta^2} - \pi l = \frac{\pi}{2}$$

or, using the definition $\beta = 4/(\epsilon^2+\delta^2)$, we have $\beta = \pi(2l+1)$. Note that at $\delta=0$,

$$\epsilon(\delta=0) = \sqrt{\frac{2}{\pi(l+\frac{1}{2})}}.$$

Moreover, from (3.3), we see that $E=-1$, for all l, there.

Since the bifurcations in these cascades occur in the same sequence on all branches, we analyze the cascade in detail for one branch, namely the $l=0$ branch. For an interval of ϵ values with $\epsilon < \epsilon_{l=0} \approx 1.2038$, the lower $l=0$ branch fixed point is stable. It is elliptic since the complex-conjugate pair of eigenvalues lie on the unit circle. However, as ϵ decreases from $\epsilon_{l=0}$ to $\epsilon^{(1)} = \sqrt{4/\pi} \approx 1.128$, the eigenvalues migrate from having $\mathrm{Re}(\lambda)=1$ to having $\mathrm{Re}(\lambda)=-1$. At $\epsilon \approx 1.128$ the fixed point becomes unstable (reflection hyperbolic), and a pair of period-2 points are created, which correspond to the $k=0$ branch of case II in Appendix B.

This process repeats itself indefinitely. The new stable period-2 points are located symmetrically with respect to the real line, say at $\pm i(\delta/2)$. It is readily shown that the eigenvalues of these period-2 points are

$$\lambda_{\pm} = -\frac{\pi^2\delta^2\epsilon^2}{2} \pm \sqrt{\frac{\pi^4\delta^4\epsilon^4}{4} - \pi^2\delta^2\epsilon^2}.$$

Also, from the geometrical interpretation of the motion undergone by a fluid particle located at the period point of the map, it is clear (see case II of Appendix B) that $4/(\epsilon^2+\delta^2)=\pi$. This last relation can, in turn, be used to find the value of ϵ, denoted $\epsilon^{(2)}$, for which $\lambda_{\pm}=-1$, i.e., when the pair of period-2 elliptic points become hyperbolic with reflection. This yields $\epsilon^{(2)} = (2/\pi)[1+\sqrt{1-1/\pi^2}] \approx 1.1136$. For ϵ just below $\epsilon^{(2)}$, a quartet of period-4 points are born. Numerically, we find that these in turn become hyperbolic with reflection and shed period-8 points at $\epsilon^{(3)} \approx 1.1118$. Although we did not pursue further bifurcations, we conjecture that a full cascade of conservative period-doubling bifurcations takes place.

It is known, see for example Helleman [1980] and Greene *et al.* [1981], that a bifurcation tree the values of the parameters at which the bifurcation actually occur scale asymptotically as

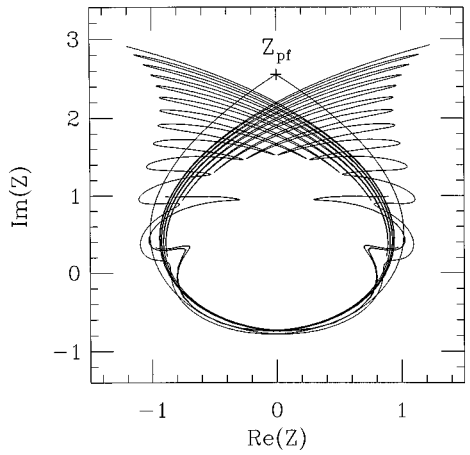

FIG. 3. The principal fixed point $\mathscr{Z}_{pf}$ and the principal homoclinic tangle formed by $W^U(\mathscr{Z}_{pf})$ and $W^S(\mathscr{Z}_{pf})$ for $\epsilon=0.39$.

$$\epsilon^{(n)}=\epsilon^{(\infty)}+\alpha\delta_F^{-n},$$

where $\delta_F\approx 8.72$ is Feigenbaum's universal constant for conservative maps. Asymptotically, for $1\ll n$,

$$\delta_F=\frac{\epsilon^{(n+1)}-\epsilon^{(n)}}{\epsilon^{(n+2)}-\epsilon^{(n+1)}}.$$

Even though we are not in the asymptotic regime, we can estimate δ_F for (2.7) from

$$\frac{\epsilon^{(2)}-\epsilon^{(1)}}{\epsilon^{(3)}-\epsilon^{(2)}}\approx 8.17$$

which is in reasonable agreement with the universal δ_F. This result supports our conjecture that a fully developed cascade of bifurcations is taking place, not only for the $l=0$ branch, but for all of the $l\geqslant 0$ branches.

IV. GLOBAL DYNAMICS

In this section, the global geometry of the map needed for the scattering results of the next section is described.

A. The principal homoclinic tangle

The relative disposition of the stable and unstable manifolds, $W^S(\mathscr{Z}_{pf})$ and $W^U(\mathscr{Z}_{pf})$, of the principal fixed point $\mathscr{Z}_{pf}$ governs almost all of the interesting dynamics of the map M. As stated in the Introduction and as shown in Fig. 3 for $\epsilon=0.39$, one branch of each of the manifolds asymptotes to infinity. The other two branches, however, intersect transversely in infinitely many points, forming a homoclinic tangle.

The splitting distance between the stable and unstable manifolds $W^S(\mathscr{Z}_{pf})$ and $W^U(\mathscr{Z}_{pf})$, which may be taken as a measure of the width of the homoclinic tangle, increases nonlinearly with ϵ. We show long portions of the unstable manifolds $W^U(\mathscr{Z}_{pf})$ for $\epsilon=0.32$, 0.39, 0.44, 0.62, 1.13 in Fig. 4, and the stable manifolds are reflections in the $\mathrm{Im}(\mathscr{Z})$-axis of the unstable manifolds. In the asymptotic limit of vanishing ϵ, the width of the tangle is exponentially small, i.e., $\mathscr{O}(e^{-c/\epsilon})$ for some $c>0$. Indeed, Fig. 4(a) shows that the tangle is extremely narrow even for $\epsilon=0.32$. By contrast, for both $\epsilon=0.39$ and $\epsilon=0.44$, the tangle already has a substantial width. Finally, for both $\epsilon=0.62$ and $\epsilon=1.13$, the unstable manifolds $W^U(\mathscr{Z}_{pf})$ (and hence also the stable manifolds) penetrate deep into the core of the vortex, see Figs. 4(d) and 4(e).

B. Stochasticity threshold and core penetration

For small values of ϵ, particles starting close to the center of the vortex remain close to it forever. They are trapped between invariant circles. For example, for $\epsilon\leqslant 0.25$, there are many, nested invariant circles inside the principal homoclinic tangle. Fig. 5(a) shows one invariant circle for $\epsilon=0.25$. These circles act as barriers that prevent particles inside from leaving the core region and particles outside from penetrating it.

However, for values of $\epsilon>0.25$, there are fewer circles and the area they occupy shrinks. Hence, particles can penetrate deeper into the core region as ϵ increases, and this is consistent with the observed increase in the width of the principal homoclinic tangle.

For $\epsilon\geqslant 0.265$ there do not appear to be any more main barriers. There are no closed circles that persist from the family of circles in the $\epsilon=0$ version of the map. As a result, it might be said that $\epsilon\approx 0.265$ is the threshold for global stochasticity, since particles can explore almost the entire core region. For example, with $\epsilon=0.265$, almost the entire region inside of the period-7 island chain appears stochastic. See Fig. 5(b) with initial condition $x_0=-0.1325$ and $y_0=1.85$ iterated 100 000 times. The only exception to the entire region appearing stochastic are, of course, the many tiny islands around periodic points of the map.

Although the main barriers are no longer present for $\epsilon\geqslant 0.265$, it is observed numerically that particles stick to certain island chains and stay inside of the associated resonance bands for many iterates. For example, for $\epsilon=0.265$, the particle initially at $\mathscr{Z}_0=2.295i$ sticks to a period-21 island chain for more than 80 000 iterates of the map. Thus, although the particular value of the control parameter ϵ is above the stochasticity threshold (and hence there are no complete barriers preventing core penetration), there are still effective barriers. This stickiness decreases when ϵ increases.

In addition, for any m:1 subharmonic periodic orbit, the phase of one of the periodic points in the orbit may readily be determined using the symmetry of the map, and the phases of the other $m-1$ points follow from the fact that they are equally spaced in the angle $\theta\equiv\tan^{-1}(\mathrm{Im}(\mathscr{Z})/\mathrm{Re}(\mathscr{Z}))$ that is conjugate to the action $I\equiv\mathscr{Z}^2/2$. This may be seen from the period-7 and period-21 elliptic orbits. However, if one attempts to calculate these phases using a perturbation series in powers of $\sqrt{\epsilon}$, then one must go to the $\mathscr{O}(\epsilon)$ equation to determine them. Observe that on average in the $\epsilon\to 0$ limit the fluid particle is in the negative-x half-plane 50% of the time and so half of the kicks it receives direct it inward onto an orbit of smaller action, while during the other 50% of the m periods it is in the positive-x half-plane, and hence the other half of the kicks force it outward onto an orbit of larger action. Furthermore, this holds for each initial phase θ_0. Thus, the $\mathscr{O}(\sqrt{\epsilon})$ correction to the action automatically

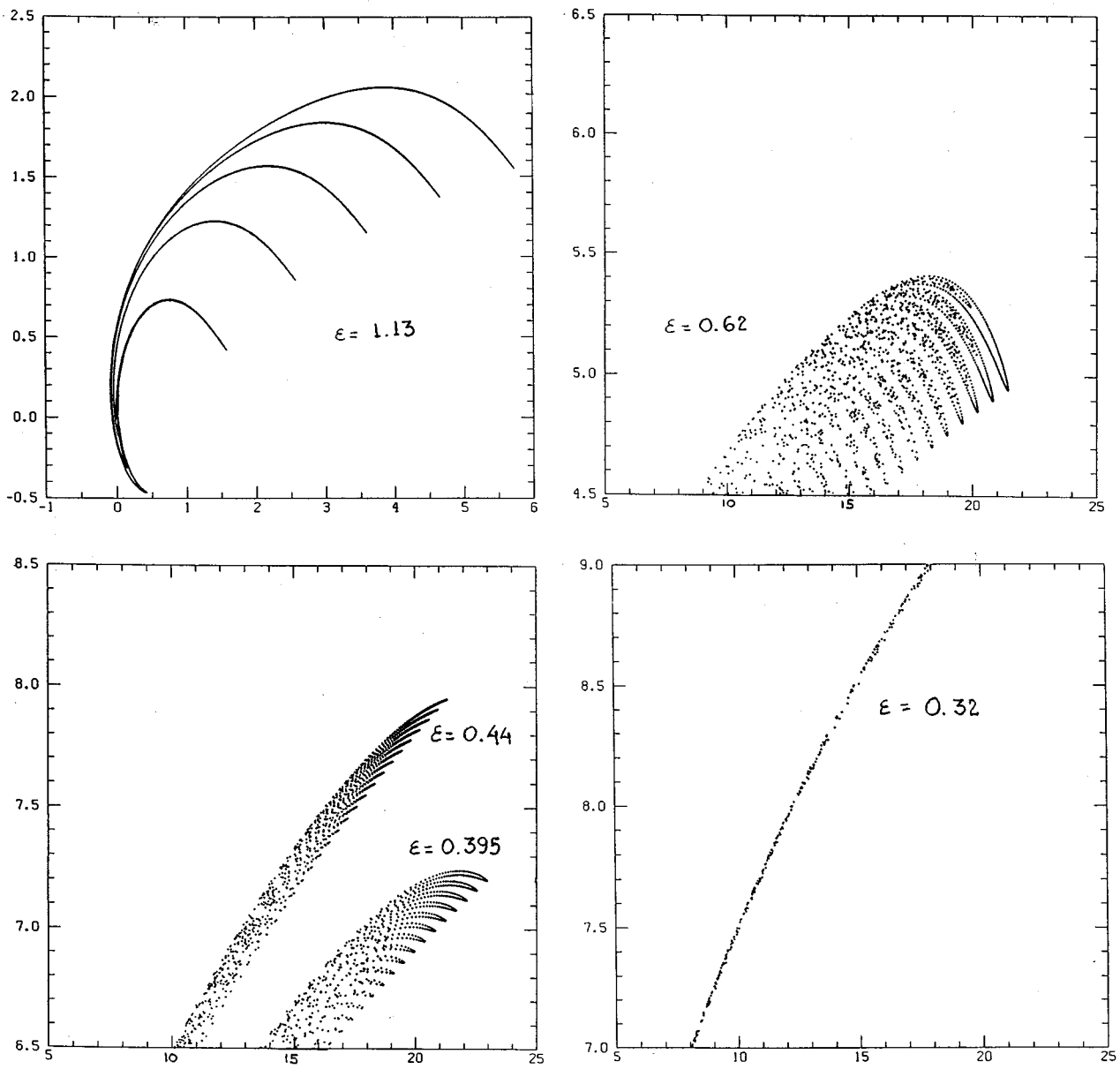

FIG. 4. The principal homoclinic tangles for ϵ=0.32, 0.39, 0.44, 0.62, and 1.13.

returns to its initial value at the end of m periods, irrespective of the initial phase, and one must use higher order equations to select θ_0. This phenomena has an analog in twist map theory.

Finally, the location of the unstable manifold of the $l=1$ saddle fixed point, which we denote by $W^U(1)$, provides another indication that particles can move deeper into the core region as ϵ increases. Figures 5(c) and 5(d) show one branch of $W^U(1)$ for ϵ=0.35 and ϵ=0.44, respectively, as well as one branch of the respective manifolds $W^U(\mathcal{Z}_{pf})$. Whereas for ϵ=0.35, the two manifolds shown stay bounded away from each other, they are very close to each other for ϵ=0.44. In fact, the inner manifold $W^U(1)$ closely follows inside the folds of the outer manifold $W^U(\mathcal{Z}_{pf})$.

V. SCATTERING

Most of the unbounded orbits of the map (2.7) that pass through or near the principal homoclinic tangle undergo chaotic scattering. Chaotic scattering plays an important role when the parameter ϵ is in the range (0.25,1.2). The measure of initial conditions which undergo chaotic scattering is near its maximum for $0.35<\epsilon<0.8$.

We begin by studying the evolution of an initial condition that is far from the origin. In particular, we take the point $\mathcal{Z}_0=-x_0+ib$, where $x_0\gg 1$ and iterate it under the map (2.7) until it crosses the line $\mathrm{Re}(\mathcal{Z})=x_0$, see Fig. 6. In general, iterates of a point such as $\mathcal{Z}_0$ will never land exactly on the line $\mathrm{Re}(\mathcal{Z})=x_0$. However, because of the smooth

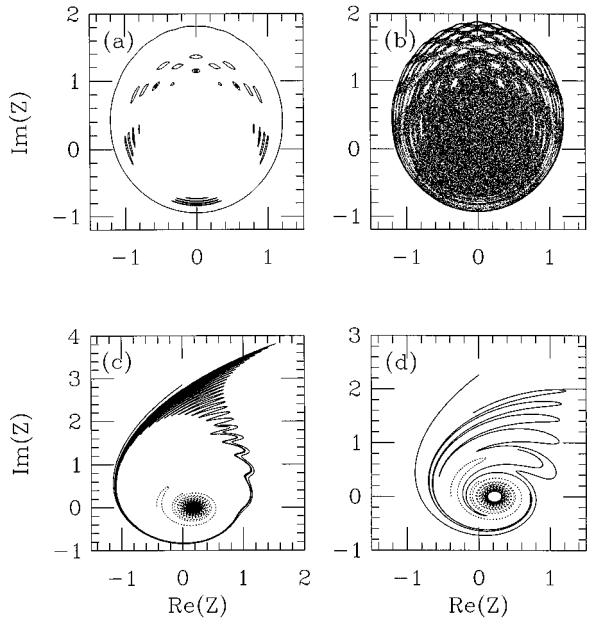

FIG. 5. (a) Invariant circle and island chains for $\epsilon=0.25$; (b) 100 000 iterations of the initial condition $x_0=-0.1325$, $y_0=1.85$ for $\epsilon=0.265$. Observe the (sticky) island chains in the outer region of the plot. No invariant circles are observed at this value of ϵ. (c) The unstable manifolds of the $l=0$ and $l=1$ saddle fixed points when $\epsilon=0.35$. The latter lies deeper in the core region, well away from the former. (d) The unstable manifolds of the $l=0$ and $l=1$ saddle fixed points when $\epsilon=0.44$. Here the latter is spread over a much larger portion of the core region than is the case when $\epsilon=0.35$, and it practically meets the former.

behavior of the trajectories far from the origin [asymptotically they behave as $y=y_0+(1/\epsilon)\ln(x/x_0)$], a linear interpolation between $\mathcal{Z}_n$ and $\mathcal{Z}_{n+1}$ [where $\mathcal{Z}_n=M^n(\mathcal{Z}_0)$, $\mathrm{Re}(\mathcal{Z}_n)\leqslant x_0$ and $\mathrm{Re}(\mathcal{Z}_{n+1})>x_0$] will allow us to assign a unique point $\tilde{\mathcal{Z}}$ for the passage of the orbit through the line $\mathrm{Re}(\mathcal{Z})=x_0$, i.e., $\tilde{\mathcal{Z}}=x_0+ib'$.

The fate of an incoming fluid particle is sensitively dependent on its initial condition. This sensitive dependence is manifested in a plot of b' as a function of b. In Fig. 7(a) we show such a plot with $\epsilon=0.39$. Three regimes can be observed. For $b<6.95$, b' is a smooth, nonmonotonically increasing function of b. For $6.95<b<7.29$, the plot of b' vs b behaves singularly (i.e., b' varies wildly for small variations in b). For $b>b^*\approx 7.29$, we have exactly $b'(b)=b$. The richest of these regimes is the second one, of which successive blowups are shown in Figs. 7(b)–7(d). Note that we chose to plot b' as a function of b to measure the scattering that the trajectories undergo rather than their asymptotic deflection angle, since the latter is always approximately zero in this system.

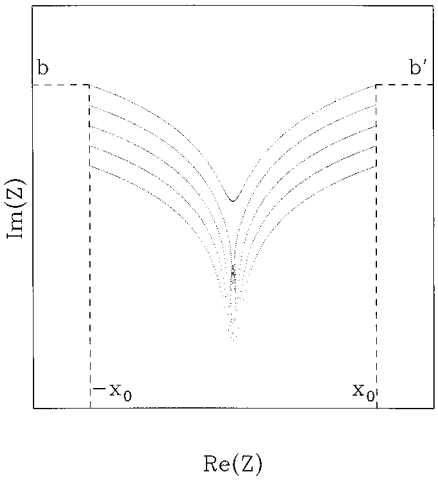

FIG. 6. Definition of the parameters b and b' used in the chaotic scattering analysis. After several iterations under the map (2.7), the point originally at $\mathcal{Z}_0=-x_0+ib$, crosses the line $\mathrm{Re}(\mathcal{Z})=x_0$ with an ordinate defined as b'.

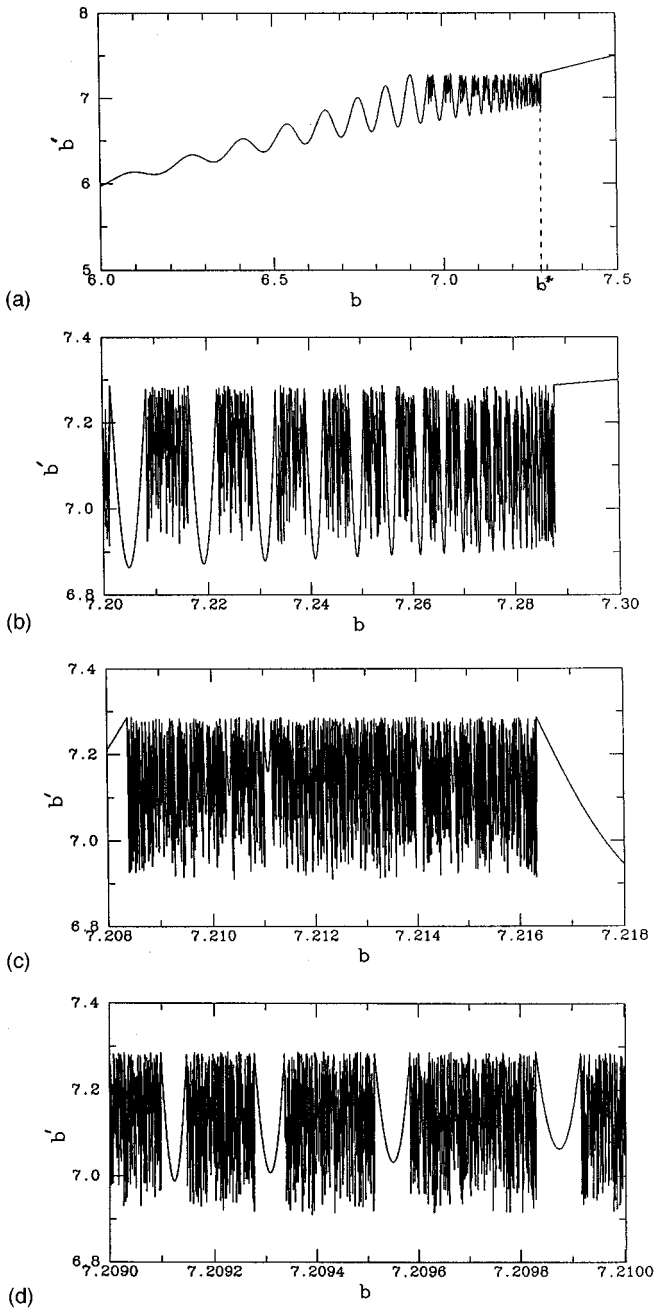

FIG. 7. Successive blowups the function b' vs b for $\epsilon=0.39$. The self-similarity is apparent. The magnification of (b), (c) and (d) with respect to (a) is 15, 150, and 1500 respectively.

Another important indicator of the chaotic scattering fluid particles undergo is the number of iterations that they

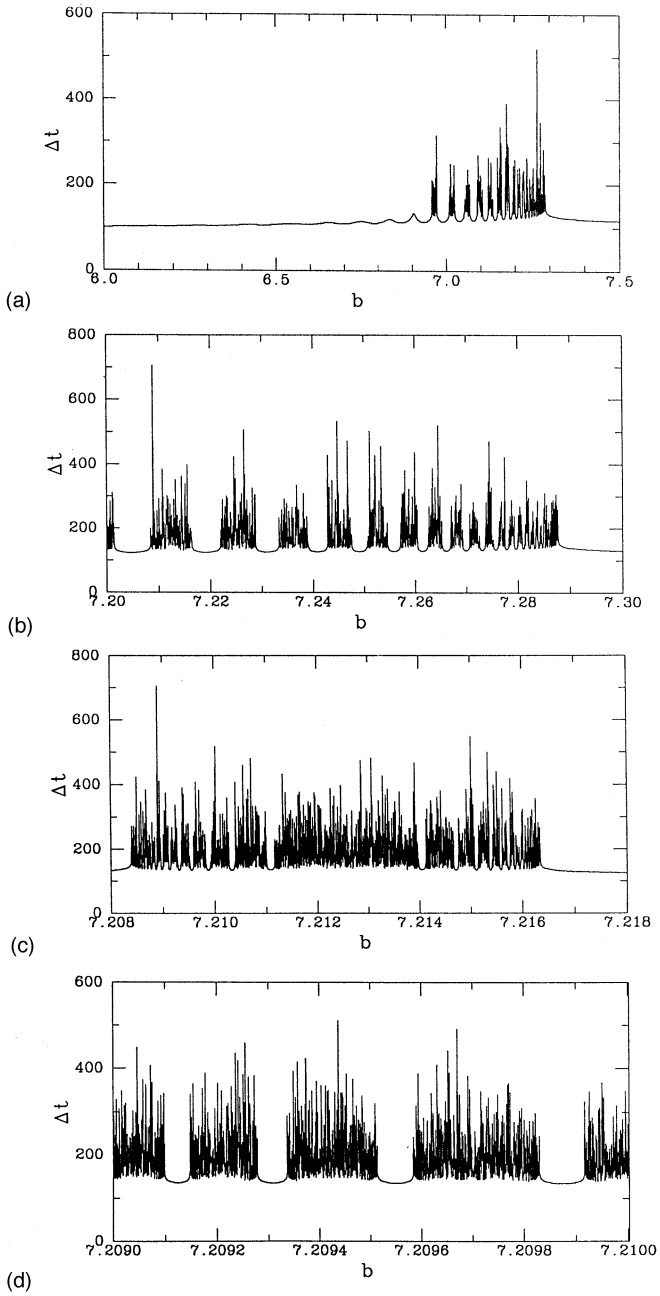

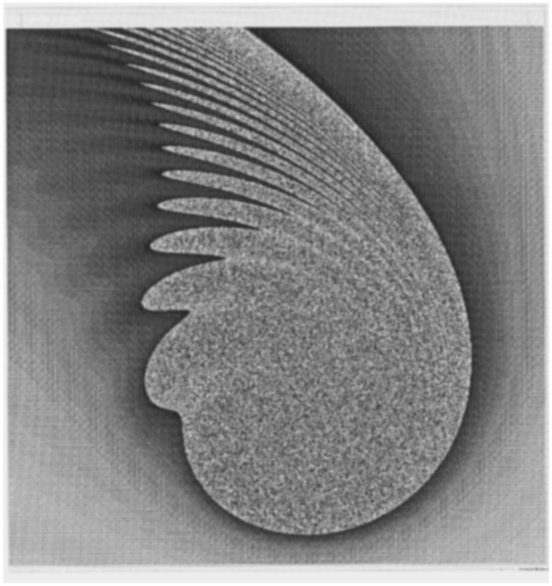

FIG. 8. (a)–(d) Successive blowups of the residence time Δt needed for a particle starting at $-x_0+ib$ to reach x_0+ib' at $\epsilon=0.39$. The sensitive dependence of the residence time on the initial condition is shown in (e) for $\epsilon=0.39$, where to each point a shade of gray is assigned that represents the time needed for that point to cross the line $x_0=10$ from left to right. It is clear that the region of the space affected by the chaotic scattering is the zone bounded by the stable manifold of the principal fixed point.

spend in a neighborhood of the origin. This time is often referred to as the residence time. Figures 8(a)–8(d) show the time delay $\Delta t(b)$ needed for a particle starting at $-x_0+ib$ to reach x_0+ib' (more precisely, $\Delta(b)=\max\{n|\mathrm{Re}[M^n \times(-x_0+ib)]\leqslant x_0\}$). This quantity also shows an irregular behavior. For the two highest resolutions shown [Figs. 7(d) and 8(d)], zones of smooth behavior can be distinguished that resemble the features of the less-well resolved Figs. 7(a)–7(c) and 8(a)–8(c). This is an indication of self similarity, i.e., that the system exhibits fractal properties.

An alternative way to study the residence time dependence on initial condition is to plot the number of iterations needed for a given point Z_0 to cross a given line $x=x_c$ as a function of Z_0. This feature is shown in Fig. 8(e), where each shade of gray represents a different exit time. It is clear that outside the region bounded by the stable manifold of the principal fixed point, the exit times behave smoothly, whereas inside that region an interesting mixing of colors takes place, indicating a sensitive dependence of the exit times on the initial condition.

In both Figs. 7 and 8, we notice that as b increases, broad irregular zones and regular zones occur in alternating succession. The width of each individual regular and irregular zone decreases as b approaches the value b^* from below. It is also clear from Figs. 7 and 8 that each regular zone has a well-defined minimum. Call the b-value of the minimum of the first regular zone b_0, of the second one b_1, and so on. Figure 9 shows a plot of b_{i+1} vs b_i. These points follow a very well-defined straight line, $b_{i+1}=d+\lambda b_i$ with $\lambda=0.84 \pm 0.04$ and where d is some real number. This means that $\delta b_i=b_{i+1}-b_i=\lambda\,\delta b_{i-1}=\ldots=\lambda^i\delta b_0$. That is to say, the distance between minima shrinks exponentially. As the distance

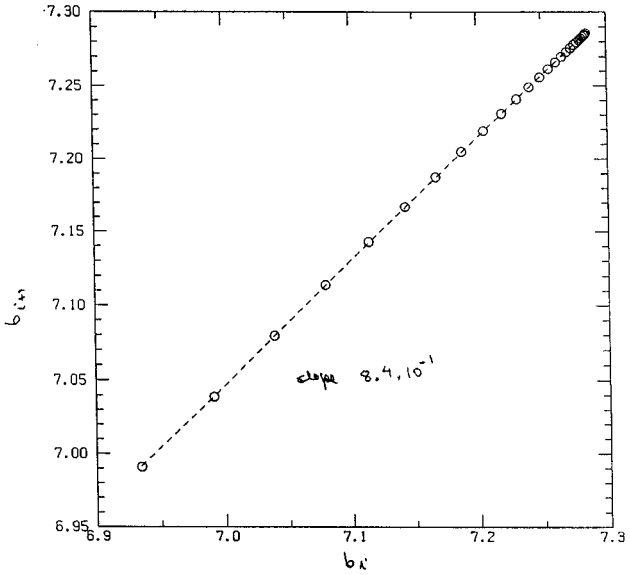

FIG. 9. Plot of b_{i+1} as a function of b_i for $\epsilon=0.39$, where b_i is abscissa corresponding of the minimum of the function of Fig. 7 (or Fig. 8) between two consecutive irregular regions, at a given resolution. The slope of the line is 0.84 ± 0.04.

between minima is a measure of the size of the irregular zone, it follows that the latter also shrinks exponentially.

The shape of the homoclinic tangle attached to the principal fixed point $\mathcal{Z}_{pf}$ and the dynamics of orbits in the tangle discussed in the previous section explain the behavior described above. Figure 10(a) shows an orbit starting at the point A, which is within the area defined by the transverse intersection of the stable and unstable manifolds that form the tangle. Upon iteration, the point jumps from one of the crests to the immediately consecutive one (going counterclockwise). At some iteration, the orbit enters the region where the homoclinic tangle lies. There, it experiences what appear to be random oscillations due to the underlying chaotic structure of the homoclinic tangle. But, unlike the bounded orbits, this orbit will eventually exit that region. Because of the strong shaking that it suffered, the final state will be sensitive to its initial condition. Figure 10(b) shows that if the incoming orbit is outside of the region occupied by the tangle, it does not enter the chaotic region. The orbit, however, will be scattered as a result of its passage through the homoclinic tangle. This is the case for the regular part of the b' vs b plots of Fig. 7.

Finally, we can also understand the behavior of b' vs b for $b>b^*$, when $b'(b)=b$. Simply, those are the orbits that start (and live) above the separatrix [see Fig. 10(b)]. Such orbits do not experience any chaotic structure (neither horseshoe nor homoclinic tangle) and then behave symmetrically.

The description given above relies heavily on the structure of the principal homoclinic tangle, see Fig. 10. However, the initial conditions used in Figs. 7 and 8 are taken at $\mathcal{Z}_0=-20+ib$. To complete the study, we use Fig. 11 which shows both a piece of the separatrix and a portion of the homoclinic tangle for $\epsilon=0.39$ in a neighborhood of the point $\mathcal{Z}=-20+ib$. From the width of the tangle and the position of the other two branches of the stable and unstable manifolds of $\mathcal{Z}_{pf}$, we immediately see why the range of irregular behavior in Fig. 7 goes from $b\approx6.8$ to $b\approx7.29$. Furthermore, we can also understand why the size of the irregular zones of the b' vs b plot shrinks exponentially (see Fig. 9). In effect, if we traverse the homoclinic tangle of Fig. 11

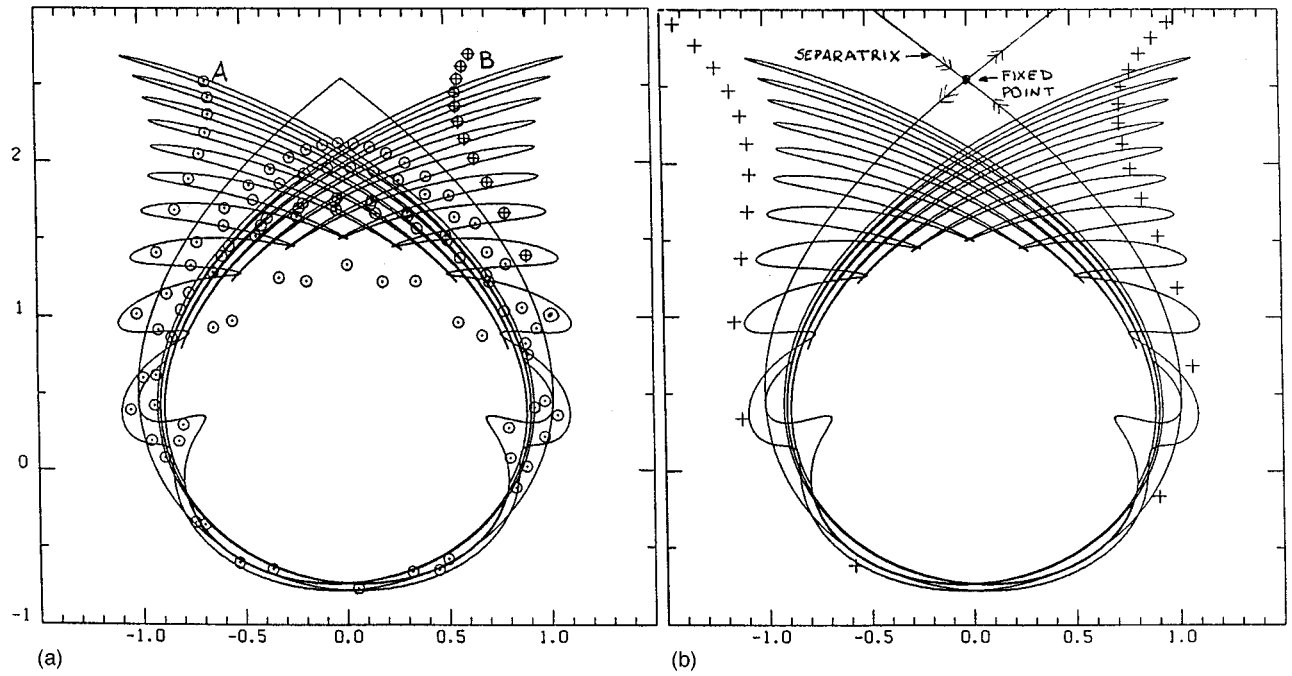

FIG. 10. (a) An initial condition starting at point A inside the lobe formed by segments of the stable and unstable manifolds experiences some chaotic shaking and some delay before leaving the neighborhood of the vortex. The subsequent evolution will see the point in the exterior lobes in the upper right. (b) An initial condition starting outside the homoclinic tangle, remains outside of it upon evolution, and does not experience any strong chaotic mixing, nor any noticeable delay.

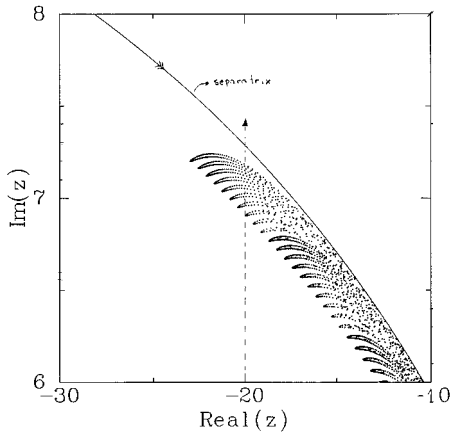

FIG. 11. A piece of the separatrix and a portion of the homoclinic tangle for $\epsilon=0.39$. At $x=-20$, only the region $6.8\leqslant y\leqslant 7.29$ is affected by the tangle. This region coincides with the range of b's that exhibit irregular behavior in Figs. 7 and 8.

vertically and upwards, we will be crossing successive regions that lie inside the homoclinic tangle, and regions that do not. If we picture the former regions as triangular shaped zones, their base will be very small and will lay on the unstable manifold, close to the fixed point. The successive bases of these ''triangles'' will shrink at a rate given by the smaller of the eigenvalues of the Jacobian of the map evaluated at the hyperbolic fixed point. For the case shown in the Fig. 9, the smaller μ of the eigenvalues is 0.82, while the slope of the curve is $\lambda=0.84$. For $\epsilon=0.34$, 0.365, 0.407, 0.51, and 0.624, the values of the smallest eigenvalues at the saddle and of this slope are, respectively: $\mu=0.89$, $\lambda=0.90$; $\mu=0.88$, $\lambda=0.91$; $\mu=0.85$, $\lambda=0.87$; $\mu=0.76$, $\lambda=0.81$; $\mu=0.68$, $\lambda=0.74$.

The above-mentioned figures showing pieces of unstable manifold near $x=-20$ also reveal that the lobes of the homoclinic tangle are nested within each other. It is this complicated and approximately self-similar nesting of the lobes far from the core that is responsible for the observed scaling properties.

The above description of the scattering properties is valid for a restricted range in the parameter ϵ. To understand how this picture changes with ϵ, it is useful to recall the history given in Sec. III of the fixed points as ϵ changes. First, for $\epsilon>1.2038$, the principal fixed point $\mathscr{Z}_{pf}$ disappears in a saddle–node bifurcation. Hence, the stable and unstable manifolds that formed the principal tangle no longer exist either. Second, the dependence of the width of the tangle on ϵ, which we illustrated in Fig. 4 for $\epsilon=1.13$, 0.62, 0.44, 0.39, and 0.32, can be used to predict the change in the shape of the b' vs b plot. For $\epsilon=1.13$, the irregular regions will occur in isolated and extremely narrow bands. These bands are wider for $\epsilon=0.62$, spanning a larger range in b-values. Finally, they get narrower again as ϵ decreases to 0.44 and 0.39. In fact, for $\epsilon=0.32$, the width of the tangle is hardly noticeable, as is expected since the splitting distance between the manifolds is exponentially small for small values of ϵ. However, a small region of irregular behavior was observed both in the b' vs b plot as well as in the time delay plot. One can expect that the irregular behavior will not be well-resolved below some value of ϵ. For example, for $\epsilon=0.14$, no chaotic scattering is observed in the b' vs b plot. The only remnant of the singular behavior at this value of ϵ is a logarithmic singularity of the time delay $\Delta t(b)$ at the value of b corresponding to the point on the upper left branch of the separatrix.

The change in the scattering properties as ϵ decreases is also related to the appearance of the other members of the hierarchy of fixed points. At $\epsilon=0.6552$, the $l=1$ fixed points appear, in a hyperbolic-elliptic pair, see Fig. 2(b). Furthermore, we recall from Sec. IV B that the homoclinic tangles of the $l>0$ fixed points interacts with the tangle of the principal fixed point for the range $0.35<\epsilon<0.655$, forming a heteroclinic structure [see Fig. 5(d) for $\epsilon=0.44$]. For this range of ϵ, the unbounded orbits entering this region experience strong mixing which is reflected in the singular part of the b' vs b plot. If we decrease ϵ even more, the principal fixed point ceases its interaction with the $l>0$ fixed points [see, for example, Fig. 5(c) in which $\epsilon=0.35$], and the only mixing affecting the irregular part of the b' vs b plot is the horseshoe structure of the principal homoclinic tangle.

VI. RESONANT CORE DYNAMICS

For small values of the control parameter ϵ (approximately $\epsilon<0.3$), the stochastic core region contains many chains of islands around fixed points and periodic points of the map M. In this section, we calculate the width of the $1:n$ superharmonic resonance zones deep inside the core. Then we use the Chirikov criterion (Chirikov [1979]) to determine the threshold parameter values at which pairs of adjacent resonances overlap. See, for example, Tabor [1989] (Sec. 4.6) for a general treatment of this criterion and an example. Also, we refer the reader to Greene [1979 a,b] for the residue method to detect the destruction of KAM tori.

The Hamiltonian in terms of action-angle variables is:

$$H(I,\theta,t)=-\ \ln\ \sqrt{I}+\epsilon\sqrt{2I}\ \sin\ \theta\sum_{k=-\infty}^{\infty}\delta(t-k).$$

Although this form of the Hamiltonian clearly exposes the role of the periodic kicking, application of the Poisson Summation Formula to it isolates each of the resonant terms. From Lighthill [1958], we have

$$\sum_{k=-\infty}^{\infty}\delta(t-k)=1+2\sum_{n=1}^{\infty}\ \cos(2\pi nt).$$

Hence, grouping terms appropriately and using the sine addition formulas, the Hamiltonian becomes:

$$H(I,\theta,t)=-\ \ln\ \sqrt{I}+\epsilon\sqrt{2I}\sum_{n=-\infty}^{\infty}\ \sin(\theta-2\pi nt). \qquad (6.1)$$

Having isolated each of the resonance terms in (6.1), we now turn to study one of them. This corresponds to fixing an integer value of n and examining an annular region about the $\epsilon=0$ invariant circle with $I=I_n\equiv 1/4\pi n$. Choosing the generating function $F(J,\theta,t)=(\theta-2\pi nt)J+\theta I_n$ facilitates this study since

$$I=\frac{\partial F}{\partial\theta}=I_n+J$$

and the resonant phase (conjugate to the action deviation J) is

$$\psi = \frac{\partial F}{\partial J} = \theta - 2\pi n t.$$

Upon averaging the Hamiltonian over the time interval 2π, all of the nonresonant phase terms vanish, so that the averaged Hamiltonian depends only on J and the slow resonant phase:

$$\bar{H}(J,\psi) = -\ \ln\ \sqrt{I_n + J} + \epsilon\sqrt{2(I_n+J)}\ \ (\sin\ \ \psi) - 2\pi n J, \tag{6.2}$$

where the last term arises since F is explicitly time dependent. Next, we may expand both of the functions of I in (6.2) about the resonant value I_n:

$$-\ \ln\ \sqrt{I} = -\ \ln\ \sqrt{I_n} - \frac{1}{2I_n} J + \frac{1}{2}\cdot\frac{1}{2(I_n)^2} J^2 + \mathcal{O}(J^3)$$

and $\epsilon\sqrt{2I} = \epsilon\sqrt{2I_n} + \mathcal{O}(\epsilon J)$. Plugging these expansions into $\bar{H}$, absorbing the constant term into the value of $\bar{H}$, shifting the resonant phase by a constant initial phase $\pi/2$, and observing that the terms linear in J cancel, we are left with precisely the normal form for the nth resonance:

$$\bar{H}(J,\psi) = \frac{1}{4(I_n)^2} J^2 + \epsilon\sqrt{2I_n}\ \ \cos\ \ \psi + \mathcal{O}(J^3, \epsilon J). \tag{6.3}$$

For all $0 < \epsilon < \epsilon_0$, where ϵ_0 depends on n, the nth resonance is isolated from the other principal resonances. Its separatrices are given by: $J_{sx}(\psi) = \pm 2I_n\sqrt{\epsilon\sqrt{2I_n}}\cos(\psi/2)$ in $\psi - J$ space. Hence the width of the resonance zone may be directly calculated as twice the maximum of $|J_{sx}|$

$$(\Delta I_n) = \sqrt{\epsilon}\, 2^{9/4} (I_n)^{5/4}.$$

Translating this width in action to a width in frequency, we get

$$(\Delta\omega)_n = \frac{d\omega}{dI}(I_n)\cdot(\Delta I_n) = \sqrt{\epsilon}\, 2^{5/4}(I_n)^{-3/4} = \sqrt{\epsilon}\, 2^{11/4}\pi^{3/4} n^{3/4}. \tag{6.4}$$

Finally, we use the above determination of the width of an isolated resonance zone to develop the Chirikov resonance overlap criterion. For this, we need (6.4) and the spacing between adjacent resonances:

$$\Delta\Omega \equiv \frac{\partial H_0}{\partial I}(I_{n+1}) - \frac{\partial H_0}{\partial I}(I_n) = 2\pi(n+1) - 2\pi n = 2\pi. \tag{6.5}$$

Chirikov [1979] established that two adjacent resonances overlap when

$$(\Delta\omega)_n = \frac{\Delta\Omega}{2}.$$

Plugging in the numbers, the Chirikov's criterion implies that the nth and $(n+1)$th resonances overlap for:

$$\epsilon \geqslant \sqrt{\frac{\pi}{2^{11} n^3}}.$$

As an example, set $n=1$, so that we determine an upper bound for the threshold value of ϵ at which the $l=0$ stable period-1 resonance zone overlaps with the $l=1$ layer:

$$\epsilon \geqslant \sqrt{\frac{\pi}{2^{11}}} \approx 0.04.$$

Numerical simulations confirm that this is approximately the threshold, and that it is a conservative estimate of the threshold.

VII. BIFURCATION AT INFINITY

The principal fixed point $\mathcal{Z}_{pf}$ is created in a bifurcation at infinity when $\epsilon = 0$. It is created as the resonant response to the $\mathcal{O}(\epsilon)$-amplitude perturbation of the circle of fixed points at infinity in the $\epsilon = 0$ system. Recall from the previous section that the blinking uniform stream contains all harmonics of the basic frequency, $n = 0, 1, \ldots$, where the $n=0$ mode is just the constant term 1. This constant term is referred to as the zero mode. Due to its presence in the blinking uniform stream, the zero frequency orbit (namely the circle of fixed points) at infinity gives rise to a 1:1 resonance band for $\epsilon > 0$.

The complete analysis is more delicate than this brief sketch and requires Poincaré compactification of $\mathbb{R}^2$. Since this is also of interest in its own right, we present it here. See for example Lefschetz [1963] or Perko [1991] for a general treatment of the technique.

We begin with the complex conjugate of the equations (2.9) in time-continuous form:

$$\dot{\bar{\mathcal{Z}}} = \frac{i\bar{\mathcal{Z}}}{|\mathcal{Z}|^2} + \epsilon\left[\sum_{k=-\infty}^{\infty}\delta(t-k)\right]. \tag{7.1}$$

In order to bring the points at infinity to a finite location in the plane, we transform to the new complex variable: $\zeta \equiv 1/\mathcal{Z}$, giving:

$$\dot{\zeta} = -i\zeta|\zeta|^2 - \epsilon\zeta^2\left[\sum_{k=-\infty}^{\infty}\delta(t-k)\right]. \tag{7.2}$$

Next, we represent ζ in its polar form $re^{i\theta}$ so that we may easily analyze the way in which trajectories approach the origin in the complex ζ plane. Substituting into (7.2) yields:

$$\begin{aligned} \dot{r} &= -\epsilon r^2\ \ \cos\ \ \theta\left[\sum_{k=-\infty}^{\infty}\delta(t-k)\right], \\ \dot{\theta} &= -r^2 - \epsilon r\ \ \sin\ \ \theta\left[\sum_{k=-\infty}^{\infty}\delta(t-k)\right]. \end{aligned} \tag{7.3}$$

This is the form of the equations which we analyze.

The dynamics near infinity in the original $\mathcal{Z}$ plane (near $r=0$) are determined as follows: For $-\pi/2 < \theta < \pi/2$, r is decreasing, and for $\pi/2 < \theta < 3\pi/2$, r is increasing. Moreover, for small r and for $0 < \epsilon \ll 1$, θ approaches zero for any initial value of θ. In particular, if $0 < \theta < \pi$, then θ decreases to zero, and if $-\pi < \theta < 0$, then θ increases to zero, since the second term in the second component of (7.3) dominates the first for small r. We note that r must be smaller than the value of r at

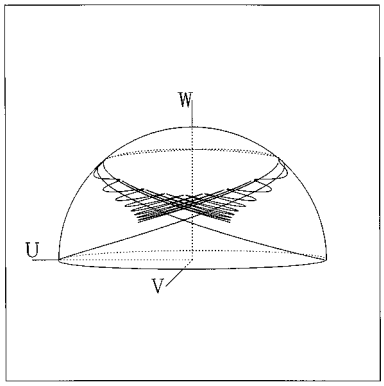

FIG. 12. Illustration of the dynamics of the stable and unstable manifolds of the principal fixed point at $\epsilon=0.39$ on the sphere $U^2+V^2+W^2=1$ induced by the Poincaré compactification presented in Sec. VII.

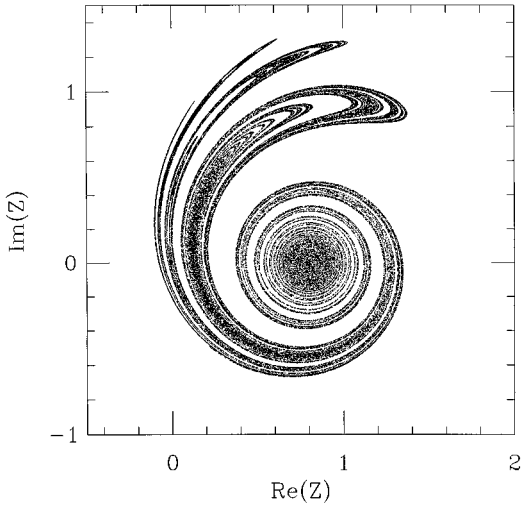

FIG. 13. A strange attractor for the map (8.1) discussed in Sec. VIII, with $\epsilon=0.8$, $\mu=2.2$, $b=0.8$, and 100 000 iterations of the initial condition $x_0=0.0$ and $y_0=0.1$.

the principal saddle fixed point. The entire phase portrait is shown on the Poincaré sphere in Fig. 12, where the coordinate axes correspond to the variables:

$$U=\frac{\mathrm{Re}(\mathcal{Z})}{\sqrt{1+|\mathcal{Z}|^2}},\quad V=\frac{\mathrm{Im}(\mathcal{Z})}{\sqrt{1+|\mathcal{Z}|^2}},\quad W=\frac{1}{\sqrt{1+|\mathcal{Z}|^2}}. \tag{7.4}$$

Now, by continuity of the vector field, we can infer the dynamics on the equator (the ''circle at infinity'') from the above analysis for small r. When $r=0$, the system has fixed points at $\theta=0$, π. The point $r=0$, $\theta=0$ is an attracting fixed point, while $r=0$, $\theta=\pi$ is a repelling fixed point. The flow on the equator of the Poincaré sphere, therefore, goes from the latter to the former, on both sides.

We observe that the above analysis is consistent with the simple physical observation that the sets of points with angular coordinates $\theta=0$ and π are the only sets of points whose angles do not get changed by the uniform stream. All points with angles between 0 and π are translated to points with smaller angle θ, while all points with angles between $-\pi$ and 0 are translated to points with larger angle θ. Thus, at infinity, where the point vortex has no rotation, we will only find fixed points at $\theta=0$ and π, and the angles of all points not initially on the x-axis must approach 0.

VIII. WEAKLY ENTRAINING VORTICES AND STRANGE ATTRACTORS

In the previous sections, the blinking vortex was taken to be an ideal point vortex, and the fluid flow was area-preserving. In this section, however, we briefly consider the weakly-dissipative map:

$$z_{n+1}=bz_n e^{i\mu/|z_n|^2}+\epsilon, \tag{8.1}$$

where $0<b<1$. While it is not our intention to study any specific compressible flows with this dissipative map of the plane, (8.1) may be considered as a paradigm map akin to the map studied in Yu *et al.* [1990, 1991]. There the dynamics of surface floaters is studied using a random two-dimensional map which is not area-preserving, yet the full three-dimensional velocity field for the fluid below the surface is incompressible. Furthermore, Yu *et al.* [1990] mention other contexts in which one gets weakly dissipative maps. Note that in (8.1), one can vary the circulation μ.

The dynamics of the dissipative map (8.1) differ both qualitatively and quantitatively from those of the area-preserving map (2.5). First, in addition to the hierarchies of fixed points and periodic points that (8.1) possesses just as (2.5) does, the map (8.1) has a circle of fixed points of radius $b\epsilon/(1-b^2)$ centered at the point $(x,y)=[-\epsilon/(1-b^2),0]$. Clearly, in the limit of $b=1$, the map (8.1) reduces to an area-preserving map of the type considered above. Moreover, in this limit, the circle of fixed points expands out to infinity.

Second, the map (8.1) appears to exhibit strange attractors. See, for example, Figure 13. These attractors are observed numerically for a wide range of parameter values for b, μ, and ϵ. The main attractors we observed numerically are created at $b=1$ in global bifurcations. The attractors appear to be the closure of the union of the unstable manifolds of the hierarchy of fixed points, given by the condition for (8.1) that is analogous to (3.2), along with the fixed points themselves. Furthermore, when the full three-dimensional velocity field is incompressible, one does not get an infinite tracer concentration on the strange attractor.

Finally, the map (8.1) is related to the Ikeda map from nonlinear optics (see Hammel [1986] and Hammel *et al.* [1985]), which has also been shown numerically to exhibit strange attractors. The Ikeda map is given by

$$w_{n+1}=Bw_n e^{i\kappa}e^{-i\alpha/|w_n|^2+1)}+\gamma. \tag{8.2}$$

We can almost attain (8.1) by setting $\kappa=0$, $B=b$, $-\alpha=\mu$, and $\gamma=\epsilon$. The only difference is the denominator of the argument of the exponential, which in the optics context cannot vanish. Hence, essential singularity at $z=0$ in (8.1) is not present in the Ikeda map. A comparison with the detailed analysis of (8.2) performed in Hammel [1986] might shed further light on the global geometry of the structures, such as the stable and unstable manifolds of the saddle fixed points, that are responsible for creating these attractors.

In addition, Romeiras *et al.* [1990], have demonstrated that small random effects do not radically change the shape of the Ikeda attractor. These random effects tend merely to make the boundary slightly fuzzy (although see Romeiras *et al.* [1990] for a full discussion of the multifractal properties of the attractors). Thus, one may expect similar results when small random noise is added to (8.1).

IX. SUMMARY AND DISCUSSION

The model presented in this paper can be a useful tool in understanding basic qualitative features pertaining to the transport of passive scalars in a number of fluid systems. As an example, we mentioned in the Introduction the intense vortical filaments that arise in turbulent flows. These linear structures are contained in the irregular field generated by the largest eddies that sweep past, as well as convect them. As a second example let us mention the long-lived ocean vortices (e.g., the Gulf Stream rings formed by the pinch off of the meanders of the Gulf Stream, Everson *et al.* [1995]) which effectively transport heat and salinity. Due to the Earth's rotation, these vortices tend to move to the west, which imparts to them a net drift velocity. As a third and final example we mention that in the opening and closing of the mitral valve of the heart, vortices are regularly cast off the valve leaflets into the oncoming periodic stream of blood (Peskin [1975]).

These three examples, as well as other fluid systems, have in common the following constituents: a vortical motion, a large scale flow and some time-dependent perturbation. The model presented in this paper is a simple version of this class of systems, in which the action of an ideal vortex is followed by the action of a uniform stream periodically. The picture that arises when these three ingredients are put together should be similar (at least for some range of parameters) to that of Fig. 10. That is, we expect a separatrix that extends to infinity, carrying along a homoclinic tangle.

The trajectories of the particles that interact with the tangle will be entrained for some time in the vortical motion, as shown in Fig. 10(a). Assimilating the particles to any passive scalar (namely temperature, concentration of a dye, etc.), it is clear that the picture sketched above suffices to produce an enhanced diffusivity for the passive scalar.

In effect, let us imagine a blob of passive particles (in a fluid at rest in infinity), and a vortex approaching at a constant speed towards this blob. When the vortex is far away, the particles are dispersed with their molecular diffusivity. However, those particles that are, at some time, in the neighborhood of the homoclinic tangle of the system will be entrained in the vortical motion, get carried along by the vortex for some residence time (which can be rather long as shown in Fig. 8), and then be eventually shed away essentially along the unstable manifold. For such a blob, the diffusivity of the passive scalar will be enhanced by the presence of vortical structures.

If we extend these ideas, the model also provides a framework for understanding enhanced diffusivity of passive scalars mixed by high Reynolds number turbulence, where a hierarchy of eddies of different scales coexist, the larger eddies convecting the smaller ones. The enhanced diffusivity in this case becomes the so-called eddy diffusivity. This enhancement of the transport properties by vortical structures lies at the heart of turbulent mixing.

The simple model that we analyzed in this paper constitutes the bare bones of the physical process just discussed. A natural context by which to analyze these issues is that of chaotic scattering. When the lengths and times are appropriately normalized, we have shown that our blinking vortex-blinking uniform stream system depends only on one parameter, namely the normalized strength of the uniform stream ϵ, defined in (2.4).

When ϵ grows from zero to being positive, an unstable fixed point is created in a bifurcation at infinity, as a resonant response to the order ϵ amplitude perturbation to the otherwise undisturbed vortex field (see Sec. VII). The fixed point so created (called here the principal fixed point) and its associated homoclinic tangle are responsible for most of the observed chaotic scattering features. The principal fixed point is one of a hierarchy of fixed points which, given the simplicity of the map, can be computed analytically [Eq. (3.2)]. Many periodic points can also be computed analytically, and we determined implicit formulas for the location of period-2 orbits (Appendix B). Some of these period-2 points participate in a hierarchy of a conservative period-doubling inverse cascade, as was discussed in Sec. III. As ϵ increases more KAM barriers disappear, and more of the vortex core becomes available to those particles that, coming from far away, get entrained in the vortex. The first stages of this process by which the vortex core becomes globally chaotic can be understood using Chirikov's resonance overlap criterion (Sec. VI). As ϵ increases, the dynamics in the vortex core changes. This dynamics determines, to some extent, the shape of the homoclinic tangle, which in turn prescribes the scattering properties of the system (Sec. V).

In summary, we studied in detail how the shape of the tangle and the core dynamics determine the chaotic scattering properties (and eventually the transport properties) for our system as ϵ is increased from zero. Eventually, for $\epsilon > 1.2038$ the principal fixed point disappears in a saddle–node bifurcation, and no further scattering is observed.

Since submission of this paper, the work of Weiss [1994] has appeared. There, a map consisting of a kicked-vortex (represented by Gaussian streamfunctions) and a uniform flow, very similar to (2.7), is analyzed. Despite the similarity of some of the results for the Gaussian and ideal point vortices, however, there is an important difference: while the ideal vortex has a divergence at $z=0$, the flow field generated by the Gaussian is smooth everywhere. While this will affect some aspects of the inner core dynamics, this does not seem to noticeably affect the main conclusions concerning the chaotic scattering properties. In this respect, the two works complement each other.

ACKNOWLEDGMENTS

We thank two anonymous referees for comments that improved the presentation of this work. In particular, we are grateful to one of the referees for bringing the references to Yu *et al.* [1990, 1991], and Romeiras *et al.* [1990] to our attention. Chris Jones introduced T. K. to the works of Ham-

mel *et al.* [1985] and Hammel [1986] before this work was started. Jones' work with Hammel was inspirational for Sec. VIII of the present paper, as well as in several indirect ways. T.K. thanks Dick Hall and Bernd Krauskopf for useful discussions. G.S. acknowledges enlightening discussions with Professor M. O. Magnasco. T.K. and L.S. gratefully acknowledge partial support from the National Science Foundation under Grant Nos. DMS-9307074 and IRI-9116451, respectively.

APPENDIX A: VARYING THE CIRCULATION

It is also of interest to vary the strength of the circulation in this idealized model. Toward this end we work with the map

$$w_{n+1}=w_n e^{i\mu/|w_n|^2}+1. \tag{A1}$$

Here the velocity of the uniform stream has been scaled to be one. A simple rescaling of the dependent variable w transforms this map (A1) into the original map (2.5). Let $\tilde{w} \equiv w/\sqrt{\mu}$. In terms of this new coordinate, the map (A1) becomes:

$$\sqrt{\mu}\tilde{w}_{n+1}=\sqrt{\mu}\tilde{w}_n e^{i/|\tilde{w}_n|^2}+1. \tag{A2}$$

Thus, dividing through by $\sqrt{\mu}$, we arrive at precisely the map (2.5) with $\epsilon = 1/\sqrt{\mu}$, and with z_n replaced by $\tilde{w}_n$.

APPENDIX B: HIERARCHY OF PERIOD-2 POINTS

The standard method to find period-2 points is based directly on the map (2.7). For each positive integer, this method finds a hierarchy of period-2 points, and can in principle be extended to find points for any integer period. Period-2 points of the map M given by (2.7) satisfy $\mathscr{Z}=M^2\mathscr{Z}$, equivalently, $M^{-1}\mathscr{Z}=M\mathscr{Z}$:

$$\left(\mathscr{Z}-\frac{\epsilon}{2}\right)e^{-i/|\mathscr{Z}-(\epsilon/2)|^2}-\frac{\epsilon}{2}=\left(\mathscr{Z}+\frac{\epsilon}{2}\right)e^{i/|\mathscr{Z}+(\epsilon/2)|^2}+\frac{\epsilon}{2}.$$

Thus, taking moduli and letting $\mathscr{Z}=\xi+i\eta$ denote a period-2 point, we get:

$$\frac{\xi+(\epsilon/2)}{\eta}=\frac{\sin\left(\dfrac{1}{(\xi+(\epsilon/2))^2+\eta^2}\right)}{1+\cos\left(\dfrac{1}{(\xi+(\epsilon/2))^2+\eta^2}\right)}. \tag{B1}$$

At this point, we have to divide the analysis in two cases, depending on whether the denominator of the previous equation is equal or different from zero.

1. Case I: $\cos(1/(\xi+\epsilon/2)^2+\eta^2)\neq -1$

The two period-2 points are located at $\pm\xi+i\eta$, i.e., symmetrically with respect to the imaginary axis. Therefore, equation (B1) must be satisfied for both $\xi+i\eta$ and $-\xi+i\eta$. This is equivalent to simultaneously solving:

$$\frac{\xi+(\epsilon/2)}{\eta}=\tan\left(\frac{1}{2[(\xi+(\epsilon/2))^2+\eta^2]}-\pi k\right), \tag{B2}$$

$$\frac{-\xi+(\epsilon/2)}{\eta}=\tan\left(\frac{1}{2[(-\xi+(\epsilon/2))^2+\eta^2]}-\pi m\right), \tag{B3}$$

where we have used double angle formulas, and k and m are positive integers.

The trajectories executed during two iterations of the map by these fixed points are the following. The fluid particle initially at $\xi+i\eta$ is transported to the right a distance $\epsilon/2$ where it then embarks on a circular trajectory, making k complete revolutions around the origin and stopping when it reaches $-\xi-\epsilon/2+i\eta$, and finally it is translated to the right by the uniform stream to the point $-\xi+i\eta$, concluding one iterate of the map. In the next iterate, the uniform stream first moves the fluid particle to the point $-\xi+(\epsilon/2)+i\eta$, from where it also embarks on a circular trajectory for ($m+a$ fraction) complete revolutions about the origin. The circular part of the trajectory ends at the point $\xi-(\epsilon/2)+i\eta$, from where the uniform stream returns it to $\xi+i\eta$, its initial position before the first iterate. From the transcendental equations (B2) and (B3), one can numerically solve for the two unknowns ξ and η as a function of ϵ for each pair of values of the parameters k and m.

2. Case II: $\cos(1/(\xi+\epsilon/2)^2+\eta^2)=-1$

Two period-2 points are located on the imaginary axis symmetrically about the origin at $\pm i(\delta/2)$. Therefore, from Eq. (B1), we have that

$$\frac{4}{\epsilon^2+\delta^2}=\pi(2l+1)$$

from whence:

$$\delta_l=\pm\sqrt{\frac{4}{\pi(2l+1)}-\epsilon^2}. \tag{B4}$$

Geometrically, these fixed points execute the following trajectories: the fixed point starting at $i(\delta/2)$ gets shifted to the right an amount $\epsilon/2$, then it makes $l+\frac{1}{2}$ turns around the origin, landing at $-\epsilon/2-i(\delta/2)$, from where it is finally transported to the right a distance of $\epsilon/2$ until it reaches the point $-i(\delta/2)$, ending the first iterate of the map. During the next iteration the particle visits $-i(\delta/2)+(\epsilon/2)$ and (after rotating $l+\frac{1}{2}$ times) $-i(\delta/2)-(\epsilon/2)$ before finally returning to its initial position at $i(\delta/2)$.

H. Aref, "Stirring by chaotic advection," J. Fluid Mech. **143**, 1 (1984).
H. Aref, "Chaotic advection of fluid particles," Philos. Trans. R. Soc. London Ser. A **333**, 273 (1990).
S. Bleher, C. Grebogi, and E. Ott, "Bifurcation to chaotic scattering," Physica D **46**, 87 (1990).
G. A. Cecchi, D. L. Gonzalez, M. O. Magnasco, G. B. Mindlin, O. Piro, and A. J. Santillan, "Periodically-kicked hard oscillators," Chaos **3**, 51 (1993).
B. V. Chirikov, "A universal instability of many-dimensional oscillator systems," Phys. Rep. **52**, 263 (1979).
P. Collet, J.-P. Eckmann, and H. Koch, "On universality for area-preserving maps of the plane," Physica D **3**, 457 (1981).
M. F. Doherty and J. M. Ottino, "Chaos in deterministic systems: Strange attractors, turbulence, and applications in chemical engineering," Chem. Eng. Sci. **43**, 139 (1988).
R. Everson, P. Cornillion, L. Sirovich, and A. Weber, "An empirical eigenfunction analysis of sea surface temperatures in the North Atlantic," submitted J. Phys. Ocean. (1994).
J. M. Greene, "A method for determining a stochastic transition," J. Math. Phys. **20**, 1183 (1979a).

J. M. Greene, ''KAM surfaces computed from the Henon-Heiles Hamiltonian,'' in *Nonlinear Dynamics and the Beam-Beam Interaction*, edited by M. Month and J. C. Herrara, AIP Conf. Proc. No. 51 (American Institute of Physics, New York, 1979b), p. 257.

J. M. Greene, R. S. MacKay, F. Vivaldi, and M. J. Feigenbaum, ''Universal behavior in families of area-preserving maps,'' Physica D **3**, 468 (1981).

J. Guckenheimer and P. Holmes, *Nonlinear Oscillations, Dynamical Systems, and Bifurcations of Vector Fields* (Springer-Verlag, New York, 1983).

S. M. Hammel, C. K. R. T. Jones, and J. V. Moloney, ''Global dynamical behavior of the optical field in a ring cavity,'' J. Opt. Soc. Am. B **2**, 552 (1985).

S. M. Hammel, ''A dissipative map of the plane—A model for optical bistability,'' Ph.D. thesis, University of Arizona, 1986.

R. H. G. Helleman, ''Self-generated behavior in nonlinear mechanics,'' in *Fundamental Problems in Statistical Mechanics V*, edited by E. G. D. Cohen (North-Holland, Amsterdam 1980), p. 165.

J. B. Kadke and E. A. Novikov, ''Chaotic capture of vortices by a moving body. I. The single point vortex case,'' Chaos **3**, 543 (1993).

S. Lefschetz, *Differential Equations: Geometric Theory*, 2nd ed. (Interscience, New York, 1963).

A. J. Lichtenberg and M. A. Lieberman, *Regular and Stochastic Motion* (Springer-Verlag, New York, 1983).

M. J. Lighthill, *An Introduction to Fourier Analysis and Generalised Functions* (Cambridge University Press, Cambridge, 1958).

E. Ott and T. Tel, ''Chaotic scattering: An Introduction,'' Chaos **3**, 417 (1993).

J. M. Ottino, *The Kinematics of Mixing: Stretching, Chaos, and Transport* (Cambridge University Press, Cambridge, 1989).

L. Perko, *Differential Equations and Dynamical Systems* (Springer-Verlag, New York, 1991).

C. S. Peskin, *Mathematical Aspects of Heart Physiology* (Courant Institute, New York, 1975).

R. T. Pierrehumbert, ''Spectra of tracer distributions: A geometric approach in nonlinear phenomena,'' in *Nonlinear Phenomena in Atmospheric & Oceanic Sciences*, edited by R. T. Pierrehumbert (Springer-Verlag, New York, 1992).

F. J. Romeiras, C. Grebogi, and E. Ott, ''Multifractal properties of snapshot attractors of random maps,'' Phys. Rev. A **41**, 784 (1990).

V. Rom-Kedar, A. Leonard, and S. Wiggins, ''An analytical study of transport, mixing and chaos in an unsteady vortical flow,'' J. Fluid Mech. **214**, 347 (1990).

Z. S. She, E. Jackson, and S. A. Orszag, ''Intermittent vortex structure in homogeneous, isotropic turbulence,'' Nature **344**, 226 (1990).

E. D. Siggia, ''Numerical study of small scale intermittency in three-dimensional turbulence,'' J. Fluid Mech. **107**, 375 (1981).

M. Tabor, *Chaos and Integrability* (Wiley–Interscience, New York, 1989).

J. B. Weiss, ''Hamiltonian maps and transport in structured fluids,'' Physica D **76**, 230 (1994).

L. Yu, E. Ott, and Q. Chen, ''Transition to chaos for random dynamical systems,'' Phys. Rev. Lett. **65**, 2935 (1990).

L. Yu, E. Ott, and Q. Chen, ''Fractal distribution of floaters on a fluid surface and the transition to chaos for random maps,'' Physica D **53**, 102 (1991).

N. J. Zabusky, D. Silver, R. Pelz, and Vizgroup93, ''Visiometrics, juxtaposition, and modeling,'' Phys. Today **46**(3), 24 (1993).

G. M. Zaslavskii and Kh.-R. Ya. Rachko, ''Singularities of the transition to a turbulent motion,'' Sov. Phys. JETP **96**, 1039 (1979).

G. M. Zaslavsky, ''The simplest case of a strange attractor,'' Phys. Lett. A **69**, 145 (1978).

G. M. Zaslavsky, ''Stochastic webs and their applications,'' Chaos **1**, 1 (1991).